AIP | Review of Scientific Instruments

Development of integrated high temperature sensor for simultaneous measurement of wall heat flux and temperature

Long Li, Jing Wang, and Xuejun Fan

Citation: Rev. Sci. Instrum. **83**, 074901 (2012); doi: 10.1063/1.4731685
View online: http://dx.doi.org/10.1063/1.4731685
View Table of Contents: http://rsi.aip.org/resource/1/RSINAK/v83/i7
Published by the American Institute of Physics.

Development of integrated high temperature sensor for simultaneous measurement of wall heat flux and temperature

Long Li, Jing Wang, and Xuejun Fan[a)]
National Key Laboratory of High Temperature Gas Dynamics, Institute of Mechanics, Chinese Academy of Sciences, No. 15 Beisihuanxi Road, Beijing 100190, People's Republic of China

(Received 17 April 2012; accepted 13 June 2012; published online 9 July 2012)

In this paper, an integrated water-cooled sensor has been developed to simultaneously measure the heat flux and temperature at the wall of a scramjet combustor. The upgrade sensor was designed based on the principle of Gardon heat-flux gauge with many improvements. The sensor was well calibrated by both conductive heating sources and blackbody cavity device. The effects of structural material and dimensions on the sensor's responses were examined. Both the experimental measurements and numerical simulation were conducted and showed that the new sensor has the maximum measure ability of heat flux of 400 W/cm^2 and stagnation temperatures up to 1920 K along with satisfactory response time. © *2012 American Institute of Physics*. [http://dx.doi.org/10.1063/1.4731685]

Nomenclature

α = thermocouple coefficient
E = output voltage of heat flux sensor
Q = heat flow
q = heat flux
R = heat resistance
σ = Stefan-Boltzmann constant in thermal radiative heat transfer
T_b = temperature of the heat sink or sensor base
T_{bc} = temperature of blackbody cavity
T_{BN} = temperature at the center of BN ceramic disk
T_c = temperature at the center of constantan disk
T_i = initial temperature of the numerical simulation field

I. INTRODUCTION

Wall heat flux and temperature are the key parameters for designing the thermal protection system of a scramjet combustor. Measurements of wall heat flux and temperature become very difficult at high flight Mach number because the sensors will face extremely hostile environment due to the excessive heat release from aerodynamic heating and combustion. For example, at flight Mach number above 6, the total temperature of air after combustion will exceed 2500 K and the average wall heat flux in the combustor ranges from 1.0 to 5.0 MW/m^2 depending on the specific fuel used (Ref.). Besides, the high temperature gases contains oxygen, which will oxidize the sensor materials very quickly. Therefore, the protection of the sensor become critical, which will determine the success and failure of the measurement.

The wall heat flux is usually measured using sensor techniques based on (1) spatial temperature gradient such as Schmidt-Boelter heat flux meter[1,2] and Gardon heat flux meter;[3,4] (2) temperature variation of a subject with time;[5,6] (3) surface heating[7] (hot-film). The sensor based on spatial temperature gradient has a good sensitivity but limited range of measurement of ~0.1 MW/m^2. The measurement range of this type of sensor could be extended greatly using a bypass heat flow path with active cooling. However, the measurement sensitivity is low and the response time is long when the heat resistances of the two heat flow paths are ill-matched. The sensor based on temperature history has a much larger measurement range of the order of 10 MW/m^2 but can only work for a few milliseconds in high enthalpy flow. The accuracy of this type of sensors is also unsatisfactory. For example, the ground tests showed that wall heat flux measured in HyShot II Scramjet combustor had an uncertainty of ~50%.[8,9]

Another difficulty related to the heat flux measurement is the sensor calibration. There are various calibrations methods,[10,11] among which the blackbody cavity[12] is the most practical one. Heat flux calibrated up to 0.5 MW/m^2 were obtained with the sensor placed outside a blackbody cavity.[13–20] Calibrations of water-cooled sensors placed inside blackbody cavity have been tested recently and maximum heat flux up to 0.5 MW/m^2 and 1.0 MW/m^2 were obtained by Murthy at NIST (Refs. 21 and 22) and Abdelmessih at Saint Martin's University,[23] respectively.

This paper is aimed to develop a high temperature sensor used to simultaneously measure the wall heat flux and temperature in supersonic combustors. The sensor was designed based on principle of Gardon heat flux gauge but much effort has been made to improve the sensor's measurement range, time response, accuracy, and durability. Recirculating water was used to cool down the sensor structure. The protection shell of the sensor was also used as a bypass heat flow path to extend the measurement range. Heat resistance analysis and numerical simulation have been carried out to help the design and optimization of the sensor structure. Calibration processes of the sensor using radiative and conductive heating were described in detail. Finally, preliminary results of the sensors tested in a Mach 2.5 Scramjet combustor were given and compared at various stagnation temperatures up to 1920 K.

[a)]Author to whom correspondence should be addressed. Electronic mail: xfan@imech.ac.cn.

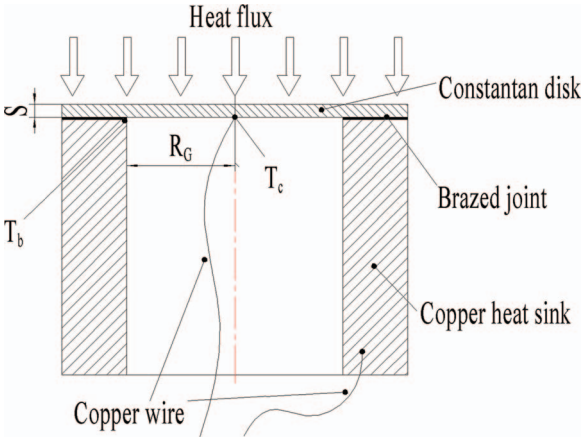

FIG. 1. Schematic of the Gardon heat flux gauge.

II. DESIGN OF HIGH TEMPERATURE WALL HEAT FLUX SENSOR

The Gardon gauge consists of a thin circular constantan disk, a copper heat sink, and a copper wire at the center of the constantan disk as shown in Fig. 1. The constantan disk was well welded at the edge of the copper heat sink. The slender copper wire, as positive electrode of output signal, was welded at the disk center. Another copper wire, as negative electrode, was connected to the copper heat sink. According to the thermocouple principle, the output voltage E is proportional to the temperature difference between the center and the edge of the constantan disk. The temperature difference is also proportional to the heat flux q applied normal to constantan disk[24]

$$E = \alpha\,(T_c - T_b) = C \cdot q, \tag{1}$$

where α is the thermocouple coefficient and C is a constant for calibration.

The heat flux sensor will be used in a high temperature environment and should be well protected. An S-shaped cooling channel was designed to cool down the copper heat sink as shown in Fig. 2. A boron nitride (BN) ceramic disk is glued on the top of the constantan disk to protect it from high temperature gases as shown in Fig. 3. The BN ceramic is machineable and has excellent electric insulation, thermal conductivity. Its working temperature can reach 2800 °C in inert gas but will reduce to 1000 °C when oxygen presents. The whole gauge is inserted tightly into a cylindrical metal shell. This metal shell is also used to bypass part of the heat flow received from the senor head in Fig. 3. With this bypass, the measurement range of the sensor will be extended significantly.

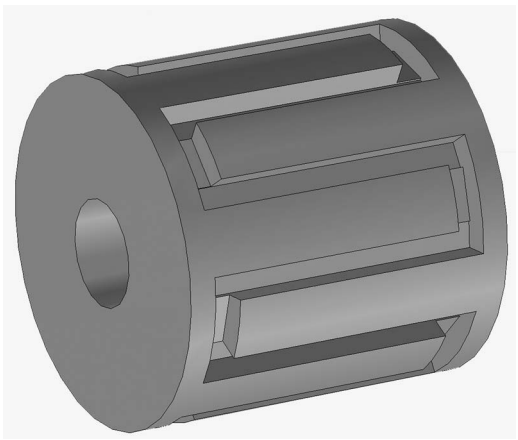

FIG. 2. The structure of cooling channels in the copper heat sink.

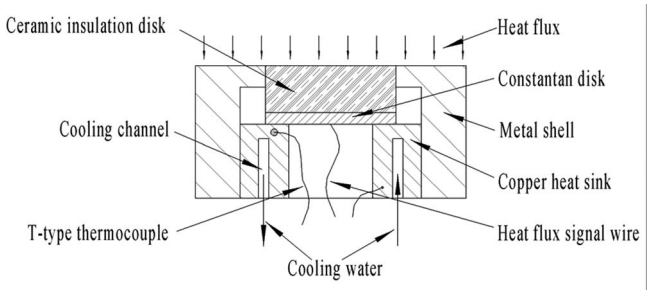

FIG. 3. Schematic of the present heat flux sensor.

It can be seen that with heat flow bypass path, the measurement range of the sensor will be extended significantly. According to Fig. 3, the total heat flow received from the senor head can be divided into two branches: the first one Q_1 flows through the ceramic and constantan disks, and the second one Q_2 flows through the metal shell, both of them converge at the copper heat sink. Assuming the heat resistances of two paths which are R1 and R2, connected in parallel, namely, $Q_2 \gg Q_1$ when $R_2 \ll R_1$, so that only little heat could flow through the constantan disk and the output signal is relatively weak; on the contrary, $Q_2 \ll Q_1$ when $R_2 \ll R_1$, thus the most of heat will flow through the constantan disk. In Sec. III, our numerical simulation to the heat conduction processes inside the sensor structure will demonstrate that the output signal of the Gardon gauge is proportional to the total heat flux received from the sensor. Consequently, the measurements with much higher levels of heat flux can be made by this type of way, in addition, its measurement range can be adjusted conveniently by varying the ratio of two heat resistances of R_1 and R_2.

III. NUMERICAL SIMULATION OF HEAT CONDUCTION INSIDE THE SENSOR STRUCTURE

Table I lists the materials and their physical properties used in the simulation.

A. Numerical simulation of heat conduction inside the constantan disk

The ANSYS 12 solver with uniform heat flux normal to its top surface was applied in the simulation. as shown in Fig. 4.

TABLE I. Physical properties of materials used in simulation.

Component	Material	Density, $\times 10^3$ (kg/m^3)	Thermal conductivity (W/m^2 K)	Specific heat capacity (J/kg K)
Insulation disk	Boron nitride	2.3	30	1600
Constantan disk	Constantan	8.9	22	410
Mental shell	Copper	8.0	400	390

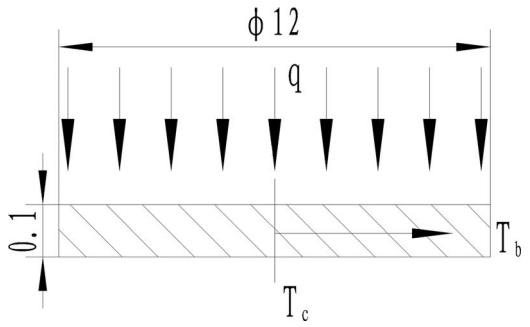

FIG. 4. Computation model of the constantan disk, all dimensions in mm.

The constantan disk has a diameter of 12 mm and a thickness of 0.1 mm. Boundary conditions of constant temperature at 300 K at the edge of the disk and adiabatic at the bottom surface is assumed. The initial condition of uniform temperature distribution ($T_i = 300$ K) is also assumed.

Figure 5 shows the steady state temperature distributions on the top surface of the constantan disk for heat flux q of 1.0 W/cm^2 and 10 W/cm^2. The calculated temperature difference between the top and bottom surfaces is very small, ~0.02 K for applied heat flux of 1 W/cm^2, which indicates that the vertical thermal conduction can be neglected and one-dimensional heat conduction assumption can be used in designing the Gardon gauge.

Figure 6 shows the temperature response at the top center of constantan disk when a heat flux of 1 W/cm^2 is applied. It shows the temperature reaches a steady state after ~6 s. Figure 7 shows the linear dependence of the steady state temperature at the center of constantan disk to the applied heat flux. It can also be seen that the maximum heat flux can be measured from this constantan disk is about 12 W/cm^2 corresponding to the maximum temperature of approximately 800 K for a T-type thermocouple according to the international standard.[25]

B. Numerical simulation of heat conduction inside the heat flux sensor

A simplified computation model of the heat flux sensor corresponding to Fig. 3 is shown in Fig. 8. The constantan disk has same dimension as in Fig. 4. Copper is chosen as the shell material. The copper heat sink and the shell are assumed to be at the same temperature of 300 K due to cooling and the initial temperature of the sensor is uniform at 300 K.

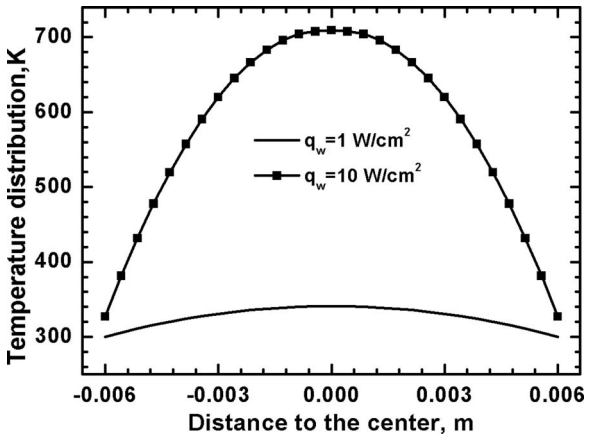

FIG. 5. Steady state temperature distributions on the top surface of constantan disk for two different heat fluxes.

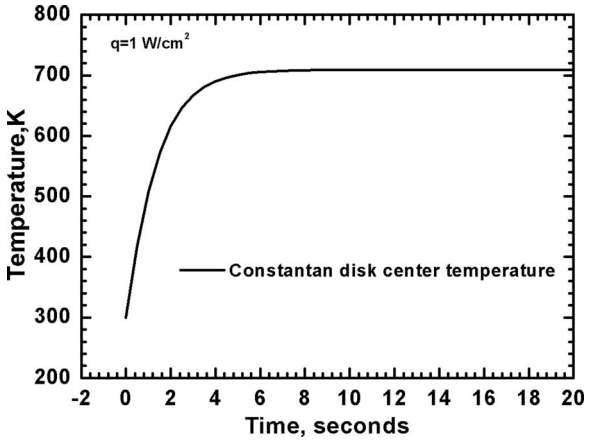

FIG. 6. Center temperature response curve of the constantan disk.

Figure 9 shows the steady state temperature contour of the simplified sensor model with a heat flux of q = 100 W/cm^2. The maximum temperature is 480 K at the center of top surface of the ceramic disk.

Figure 10 shows the steady state temperature distributions at the top surfaces of constantan and BN ceramic disks with a heat flux of 100 W/cm^2. Compared to Fig. 5 the temperature at the surface of constantan disk becomes lower for the same heat flux due to the addition of copper shell and ceramic disk.

Figure 11 shows the temperature response at the top center of the constantan disk when a heat flux of 100 W/cm^2 is applied. The response time is ~8 s, a little longer than that in Fig. 6.

Figure 12 shows the linear dependence of the steady state temperatures at the top centers of constantan and BN ceramic disks to the applied heat flux. The two profiles can be fitted linearly as following:

$$T_c = C_1 q + T_b, \tag{2}$$

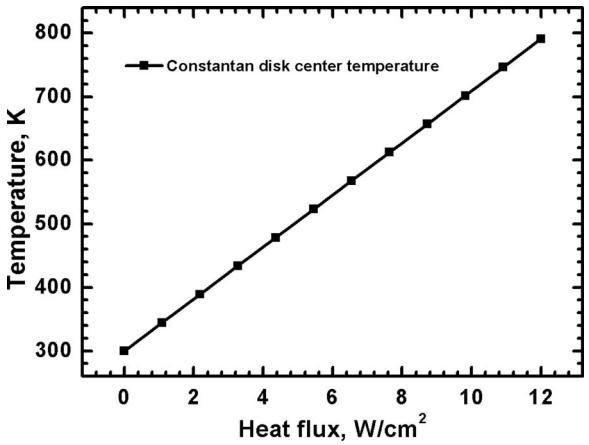

FIG. 7. Steady state temperature at the center of constantan disk as a function of applied heat flux.

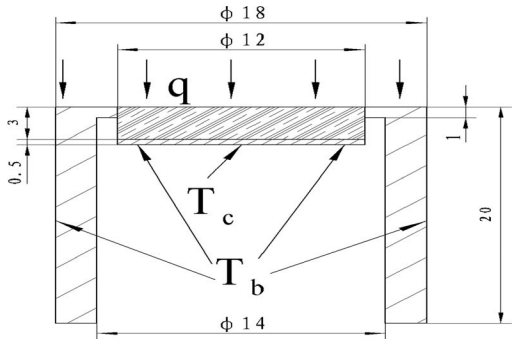

FIG. 8. Simplified computation model for the heat flux sensor in Fig. 3. All dimensions in mm.

$$T_{\mathrm{BN}} = C_2 q + T_b, \tag{3}$$

where T_c is the temperature at the center of constantan disk, T_b is the temperature of copper heat sink, T_{BN} is the temperature at the center of BN ceramic disk, and C_1 and C_2 are the proportional constants. It can be seen from Fig. 12 that the maximum heat flux can be measured from this constantan disk is about 400 W/cm^2 corresponding to the maximum constantan temperature of ~800 K, which is much higher than the maximum heat flux of 12 W/cm^2 that a Gardon gauge can measure.

C. One-dimensional heat resistance analysis of the sensor for optimization

According to the previous numerical simulation, heat flux measurement range and response time are strongly influenced by structure and material of the insulation disk and conduction shell. In order to get appropriately strong signal during each measurement, sensor with different range is needed for the different heat flux measurement environment. For example, heat flux in the isolator of a supersonic combustor is usually below 100 W/cm^2 but it will reach even up 500 W/cm^2 at combustor.

When measured heat flux intensity changes, heat resistance analysis is taken to adjust the proportion of the two resistance value and to make sure that the sensor works at best measurement range. Analysis of a sensor with a maximum measurement range has been taken in following as an example.

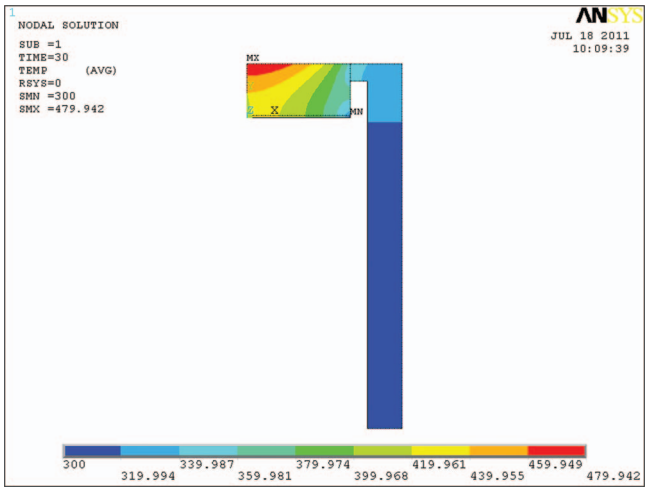

FIG. 9. Steady state temperature contour of the sensor.

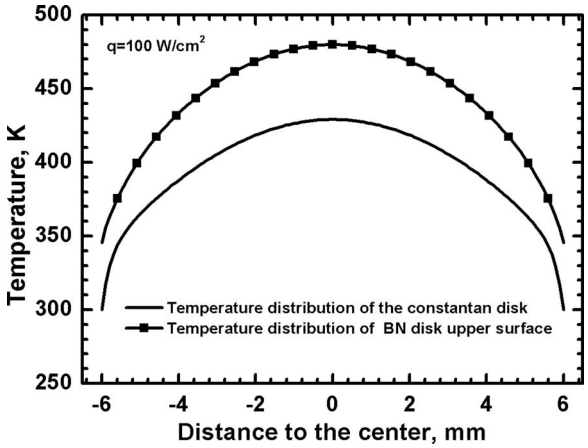

FIG. 10. Steady state temperature distributions at the top surface of constantan and BN ceramic disks.

Figure 14 shows thermal resistance network for the present sensor. Total heat flow Q makes total temperature ΔT difference because of the total resistance R.

There are three resistances on the first path, BN ceramic insulation disk R_{11}, thermal conductive layer R_{12} and constantan disk R_{13}, all of which are in series.

For BN ceramic insulation disk R_{11}, thermal conductivity $\lambda_{11} = 30$ W/(m K), thickness $l_{11} = 3$ mm, diameter $d_{11} = 12$ mm, heat resistance

$$R_{11} = \frac{l_{11}}{\lambda_{11} A_{11}} = 0.885 \text{ K/W}. \tag{4}$$

As BN and constantan do not touch perfectly, high temperature thermal conductive glue is filled between them to drive air away. Conductivity of the glue is about $\lambda_{12} = 5$ W/(m K), thickness is about 0.1 mm, $l_{12} = 0.1$ mm, diameter $d_{12} = 12$ mm, then the resistance

$$R_{12} = \frac{l_{12}}{\lambda_{12} A_{12}} = 0.177 \text{ K/W}. \tag{5}$$

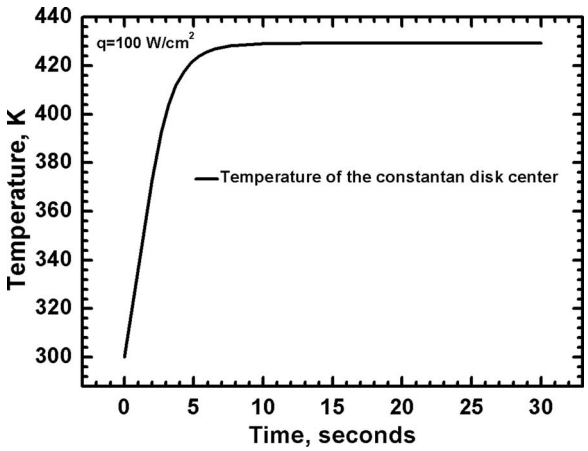

FIG. 11. Temperature response curve at the center of constantan disk.

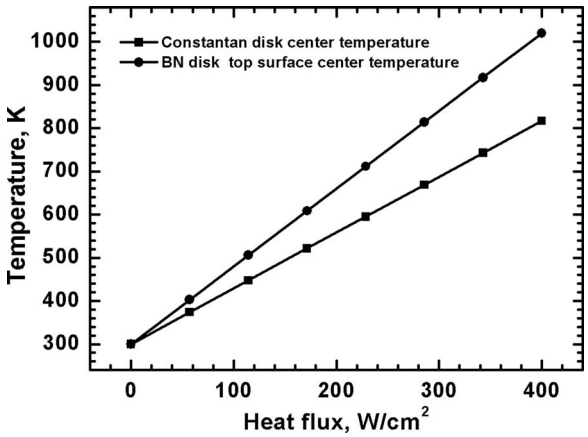

FIG. 12. Temperatures at the top centers of constantan and BN disks as a function of applied heat flux.

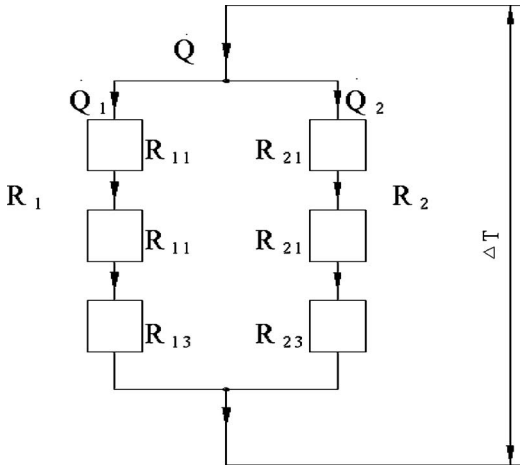

FIG. 14. Schematic of heat resistance network of the present sensor.

Conductivity of constantan $\lambda_{13} = 22$ W/(m K), thickness $l_{13} = 0.1$ mm, diameter $d_{13} = 12$ mm, according to Gardon gauge theory, thermal resistance of constantan disk is

$$R_{13} = \frac{1}{4\pi\lambda_{13} l_{13}} = 36.19 \text{ K/W}. \tag{6}$$

Total heat resistance on the first path

$$R_1 = R_{11} + R_{12} + R_{13} = 37.25 \text{ K/W}. \tag{7}$$

In the second path, as shown in Fig. 13, copper shell's resistance is divided into two parts, they are in series. A thin air layer needs to be considered though the shell touches tightly with the heat sink.

Thermal conductivity of shell 1 $\lambda_{21} = 400$ W/(m K), thickness $l_{21} = 1$ mm, outer diameter $d_{21Out} = 18$ mm, inner diameter $d_{21In} = 12$ mm, thus the heat resistance is

$$R_{21} = \frac{l_{21}}{\lambda_{21} A_{21}} = \frac{l_{21}}{\lambda_{21} \frac{\pi}{4} \left(d_{21Out}^2 - d_{21In}^2\right)} 0.018 \text{ K/W}. \tag{8}$$

For shell 2, thermal conductivity $\lambda_{22} = 400$ W/(m K), characteristic length $l_{22} = 10$ mm, outer diameter $d_{22Out} = 18$ mm, inner diameter $d_{22In} = 14$ mm, thus shell 2's thermal resistance

$$R_{22} = \frac{l_{22}}{\lambda_{22} A_{22}} = \frac{l_{22}}{\lambda_{22} \frac{\pi}{4} \left(d_{22Out}^2 - d_{22In}^2\right)} = 0.249 \text{ K/W}. \tag{9}$$

Though copper shell and heat sink make an mechanical interface fit, small areas of air gaps still exist during real manufacture. These gaps are considered ideally to be a ring column model and heat flows from the outside into inside. Air's conductivity $\lambda_{23} = 0.025$ W/(m K), characteristic thickness $l_{23} = 0.01$ mm, inner diameter $d_{23} = 14$ mm, characteristic height $h_{23} = 20$ mm. Areas of outer and inner plane can be considered to equal as the column is very thin. Then thermal resistance of the air layer

$$R_{23} = \frac{l_{23}}{\lambda_{23} A_{23}} \approx \frac{l_{23}}{\lambda_{23} \pi d_{23} h_{23}} = 0.455 \text{ K/W}. \tag{10}$$

Total thermal resistance on the second path is

$$R_2 = R_{21} + R_{22} + R_{23} = 0.722 \text{ K/W}. \tag{11}$$

Based on parallel thermal resistance, total thermal resistance of the network is

$$R = \frac{R_1 R_2}{R_1 + R_2} = 0.708 \text{ K/W}. \tag{12}$$

Assuming temperature of the heat sink is constant, $T_b = 300$ K and the max working temperature of constantan disk $T_{cmax} = 800$ K according to T-type thermocouple standard,[25] temperature difference between the constantan disk center and edge is

$$\Delta T_{13\,\max} = T_{c\,\max} - T_b = 500 \text{ K}. \tag{13}$$

The maximum heat flow can be obtained

$$Q_{13\,\max} = \frac{\Delta T_{13\,\max}}{R_{13}} = 13.82 \text{ W}. \tag{14}$$

According to thermal resistance in series,

$$Q_{1\,\max} = Q_{11\,\max} = Q_{12\,\max} = Q_{13\,\max} = 13.82 \text{ W}. \tag{15}$$

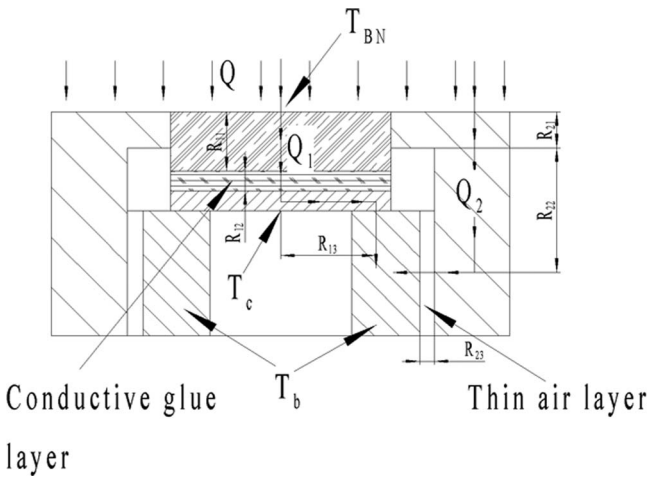

FIG. 13. Schematic of heat conduction in the sensor.

According to parallel thermal resistance, in the second path

$$Q_{2\max} = \frac{Q_{1\max} R_1}{R_2} = 713.0 \text{ W}. \quad (16)$$

Again with resistance in series,

$$Q_{2\max} = Q_{21\max} = Q_{22\max} = Q_{23\max} = 713.0 \text{ W}. \quad (17)$$

Total heat flow in the sensor is

$$Q_{\max} = Q_{1\max} + Q_{2\max} = 726.8 \text{ W}. \quad (18)$$

Sensor's diameter $d = 18$ mm, thus the maximum heat flux that sensor can measure is

$$q_{\max} = \frac{Q_{\max}}{A} = \frac{Q_{\max}}{\frac{\pi}{4}d^2} = 285.6 \text{ W/cm}^2. \quad (19)$$

The maximum temperature difference of the sensor is

$$\Delta T_{\max} = Q_{\max} R = 514.6 \text{ K}. \quad (20)$$

According to parallel thermal resistance, temperature differences on two paths are equal

$$\Delta T_{\max} = \Delta T_{2\max} = \Delta T_{1\max} = 514.6 \text{ K}. \quad (21)$$

Then the maximum temperature of the sensor upper surface is

$$T_{\text{BN}\max} = T_b + \Delta T_{\max} = 814.6 \text{ K}. \quad (22)$$

According to the one-dimensional thermal resistance analysis, measurement range of the sensor in such a structure is about 285.6 W/cm^2 and the maximum temperature will be 814.6 K. This result is comparable to the numerical simulation in Sec. III B.

The method of thermal resistance analysis can be used conveniently to design and optimize the sensor structure. For example, a desired measurement range could be obtained by properly choosing the materials and sizes of sensor shell or insulation disk.

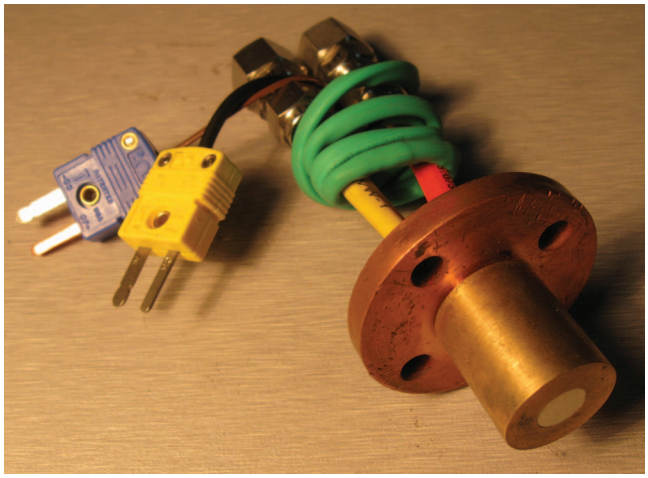

FIG. 15. Photograph of the integrated sensor for wall heat flux and temperature measurements.

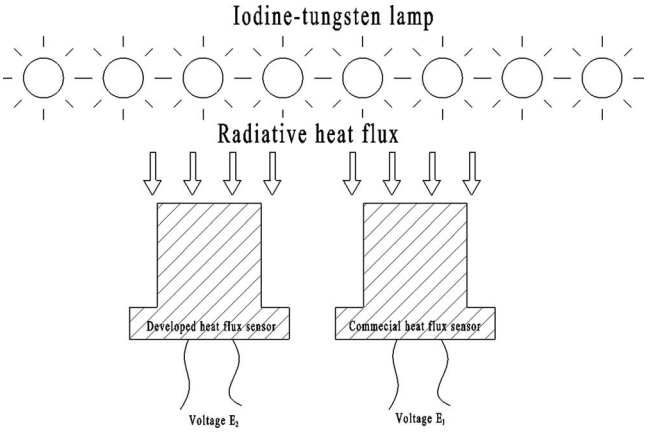

FIG. 16. Sensor calibration using tungsten iodine lamps.

IV. CALIBRATIONS OF THE INTEGRATED HEAT FLUX AND TEMPERATURE SENSOR

Figure 15 shows the picture of integrated wall heat flux and temperature sensors. The thermal conduction shell was made from brass. The diameters of the shell and the BN disk are 18 mm and 12 mm, respectively.

A. Low heat flux calibration of the integrated sensor

The heat flux sensor was first calibrated using a radiation heating device consisting of 10 tungsten iodine lamps as shown in Fig. 16. The maximum power of each lamp is 2 kW. A standard commercial heat flux meter was used to calibrate the present sensor. The calibration result is plotted in Fig. 17. It can be seen from the figure that the sensor's output voltage varies linearly with the applied heat flux. A sensitivity of 7.57 W/cm^2 mV with a relative error of 1.7% was obtained from the calibration. The maximum heat flux limited by the power of lamps in the calibration was approximately 10 W/cm^2. Calibration with higher heat flux using blackbody cavity will be described later.

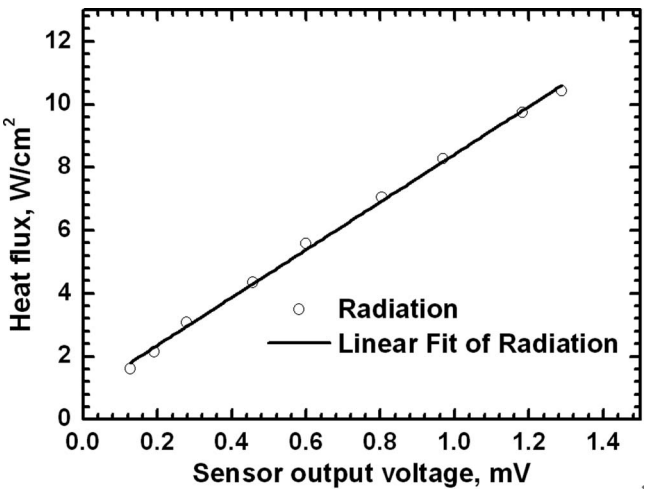

FIG. 17. Calibration curve of heat flux vs. sensor's output voltage.

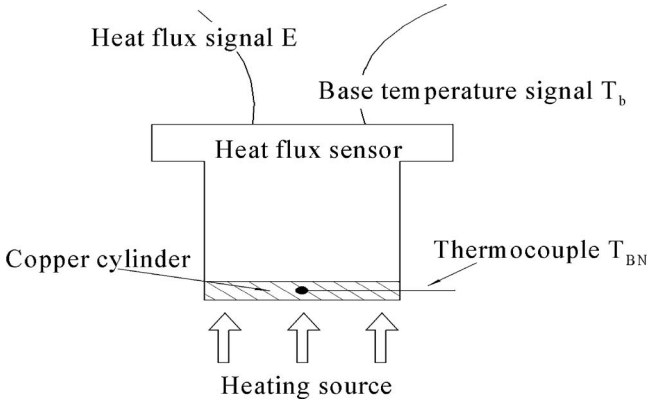

FIG. 18. Schematic of the wall temperature calibration device.

B. Method to determine the top wall temperature of the heat flux sensor

The wall temperature measurement in scramjet combustor is a crucial problem due to many well-known reasons. However, the average wall temperature at the top surface of sensor can be obtained from the heat flux measurement if the correlation exists between them. As shown in Fig. 12, the measured heat flux q is proportional to the temperature difference between the top center of the BN ceramic disk and the copper base due to Eq. (3)

$$q = C_2(T_{\mathrm{BN}} - T_b). \tag{23}$$

According to thermocouple equation (1), Eq. (23) can be written as

$$T_{\mathrm{BN}} - T_b = C_3 \cdot E, \tag{24}$$

where C_3 is a constant which can be calibrated by the measurements of T_{BN}, T_b, and E.

Figure 18 shows the consideration for the wall temperature calibration. The wall temperature at the top of heat flux sensor is measured using a thermocouple inserted into a thin copper cylinder which was mounted tightly on the top of the sensor. An electric heating source was used to heat up the copper cylinder. The data of heat flux signal E and the base temperature T_b along with the wall temperature T_{BN} were acquired simultaneously while the cylinder body was heated up to required temperature. Figure 19 plots the variation of $T_{\mathrm{BN}} - T_b$ with the output voltage of heat flux sensor. It shows a good linearity with the linear coefficient C_3 of ~49.1 K/mV with a relative error of 0.73%.

C. Effects of sensor materials and dimensions

There are many factors which will affect the response characteristics of the heat flux sensor. Figure 20 compares the response signals of heat flux sensors with different shell materials and insulation thickness. It can be seen that the bare sensor without any shell and insulator has the highest signal level and the fastest time response. In addition, sensor with a copper shell has the fastest response time but the lowest signal level. When shells were made from aluminum, brass and stainless steel, the time response tends to decreasing and the signal level increasing due to the decreasing of the material's conductivity. On the other hand, the response signal level of the sensor with 2 mm BN insulation is approximately twice of that with 3 mm BN insulation.

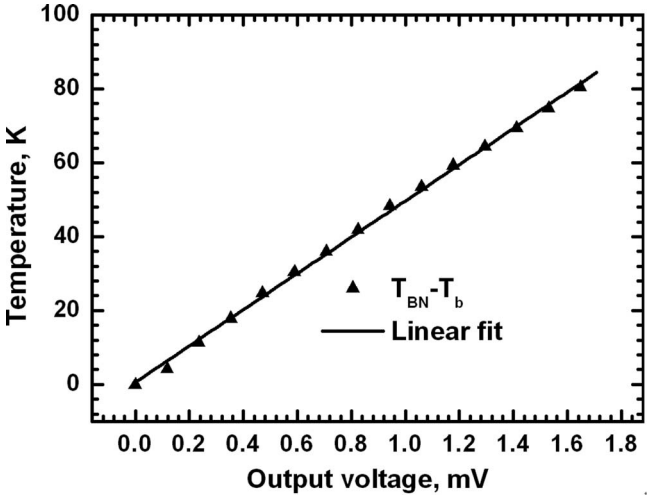

FIG. 19. Calibration curve of the temperature difference in Eq. (23) vs. the sensor's output voltage.

D. Sensor calibration using blackbody cavity

The calibrations of the sensor at the circumstance of high temperature and high heat flux, a new calibration system using blackbody cavity has been designed and fabricated as shown in Fig. 21.

The key component of the blackbody cavity is a graphite tube with an inner diameter of 30 mm and an outer diameter of 40 mm. The tube is divided equally into two cavities using a graphite disk of 5 mm in thickness, and is installed inside a stainless steel cylinder of 680 mm long and 400 mm in diameter. Thermal insulation material is filled in the space between the graphite tube and the outside cylinder. Two brass flange

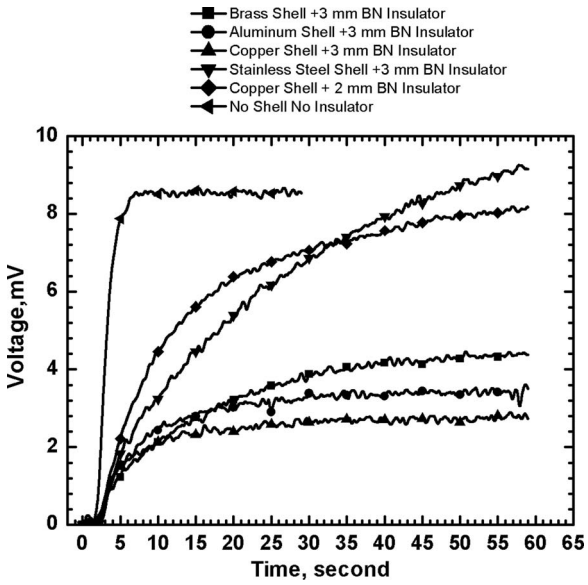

FIG. 20. Response signals for sensors with different structures.

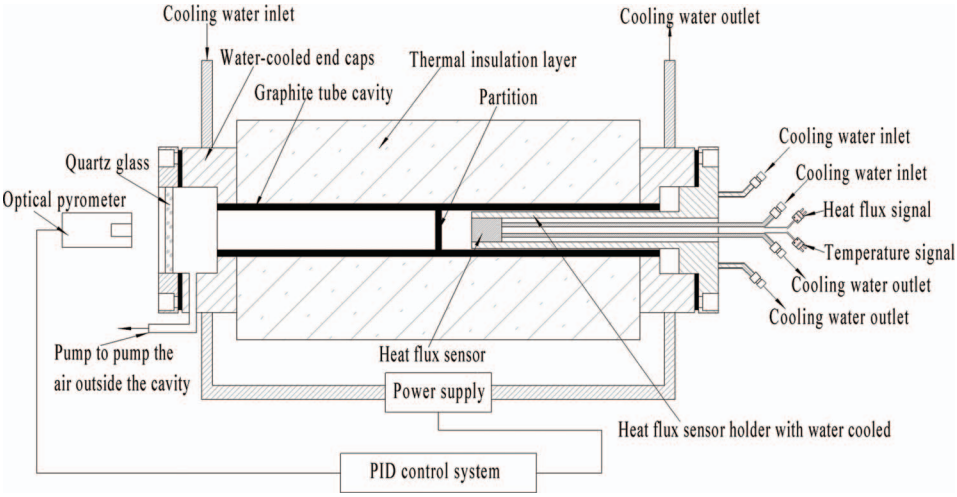

FIG. 21. Schematic of the blackbody cavity calibration system.

brackets installed at the ends of the graphite cube which are used as the electrodes of the power supply. Circulating water is used to cool down the electrodes. A high temperature optical pyrometer (MODLINE 5, Infrared Thermometer Sensor) with a measurement range of 750–3000 °C is used to monitor the cavity temperature through a quartz glass window installed at the left end of the cavity. The output signal of the pyrometer is connected to a proportional integral derivative (PID) controlling system to control the heating power. The graphite tube is heated with a low voltage of 14 V and large current of 1000 A. Air is evacuated first and pure argon is filled into the furnace to prevent the structure from oxidation at high temperature. In order to obtain a much higher heat flux, the heat flux sensor is inserted into the tube at a distance of 30 mm from the partition disk. The sensor for calibration is protected from high temperature inside cavity using a water cooled sleeve made of stainless steel. The top surface of the sensor is coated with soot to obtain an emissivity of ~0.95, such that the heat flux applied to the sensor could be estimated using the law of blackbody radiation

$$q = \sigma \left(T_{bc}^4 - T_{\mathrm{BN}}^4\right), \tag{25}$$

where $\sigma = 5.67 \times 10^{-8}$ W/m^2 K^4 is the Stefan-Boltzmann constant, T_{bc} is the temperature of blackbody cavity, and T_{BN} is the temperature on the top surface of sensor. With water cooling the temperature T_{BN} is less than half of the temperature of blackbody cavity T_{bc}, thus $T_{\mathrm{BN}}{}^4 = T_{bc}{}^4$, radiation heat flux could be approximated within an uncertainty of few percentage by

$$q \sim \sigma T_{bc}^4. \tag{26}$$

The blackbody cavity can be heated from 750 °C to 2500 °C, which corresponds to a heat flux of 8–350 W/cm^2.

Figure 22 shows the profile of experimental calibration for the heat flux sensor. Linear dependence of the sensor's output voltage on the applied heat flux can be observed for the radiation heat flux which is less than ~100 W/cm^2. The calibration coefficient from Fig. 22 is ~0.0492 mV/(W/cm^2) with a relative error of 0.09%.

V. MEASUREMENTS OF THE WALL HEAT FLUX AND TEMPERATURE IN A SUPERSONIC MODEL COMBUSTOR

Preliminary measurements were carried out in a Mach 2.5 supersonic model combustor (Fig. 23) with liquid kerosene fuel at total temperature varying from 1100 to 2000 K and total pressure of ~1.4 MPa. The combustor was cooled with recirculating water to maintain the experiment time beyond 200 s. There total seven heat flux/temperature sensors were tested which are installed along the centerline of the top combustor wall as shown in Fig. 23.

Figures 24 and 25 show the time histories of the measured wall heat fluxes and temperatures during a single run at fuel equivalence ratio of 0.67, total temperature of 1650 K, and total pressure of 1.4 MPa. In order to measure the wall heat fluxes without combustion, the liquid kerosene fuel was injected at the 20th s. It can be seen from the figures that both the heat fluxes and wall temperatures at all locations reach steady states after ~10 s. The outputs from the five sensors installed in combustion section reach to the second steady states after another 10 s when fuel was injected, while the outputs

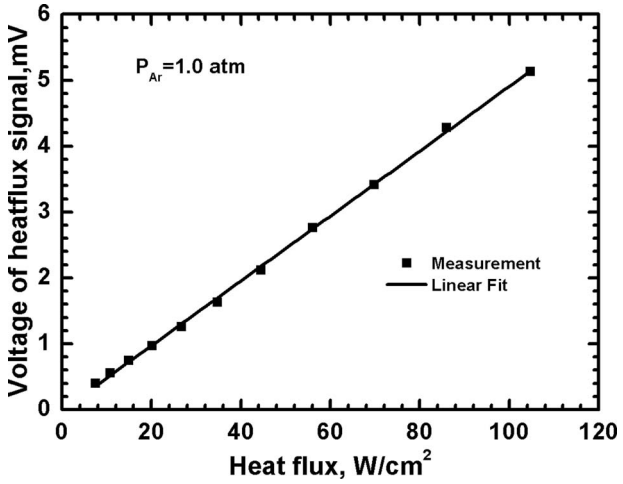

FIG. 22. Blackbody calibration curve for the heat flux sensor.

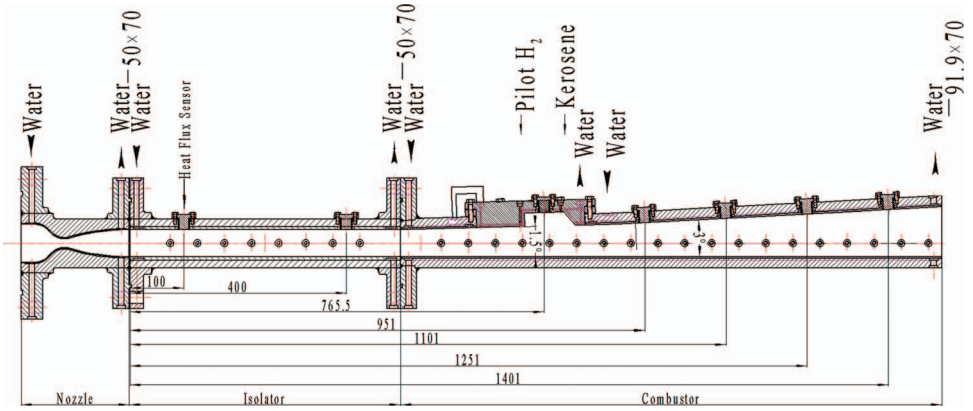

FIG. 23. Sketch of the water cooled supersonic model combustor.

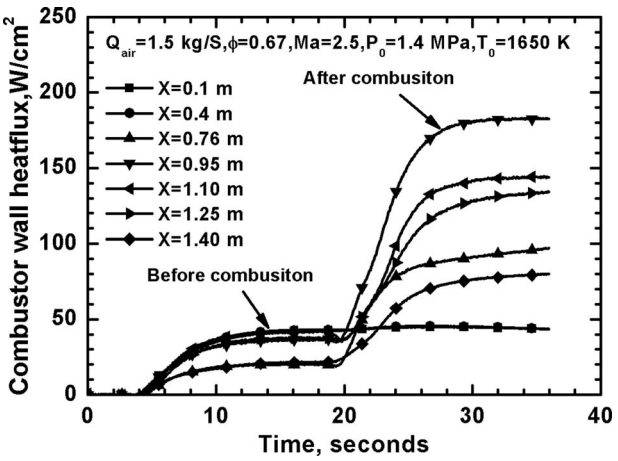

FIG. 24. Time histories of the wall heat fluxes along the combustor.

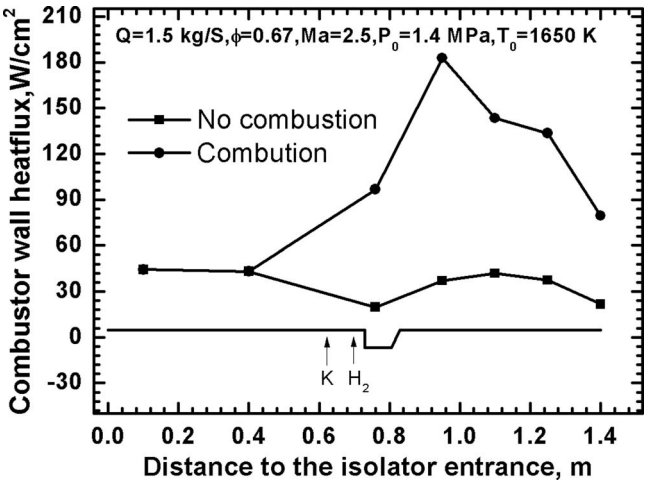

FIG. 26. Heat flux distributions along the combustor with and without combustion.

from the first two sensors installed in the isolator remain almost constant.

Figure 26 compares the wall heat flux distributions at the 16th (no combustion) and 36th s (combustion). The maximum heat flux with combustion increases ~4–5 times. The peak heat flux appears just downstream the cavity. Figure 27 shows the corresponding wall temperature distributions for the two cases. The wall temperatures with combustion is nearly twice as much as that without combustion in the combustion region. Most of the sensors survived after about 50 runs and the outputs showed very good repeatability.

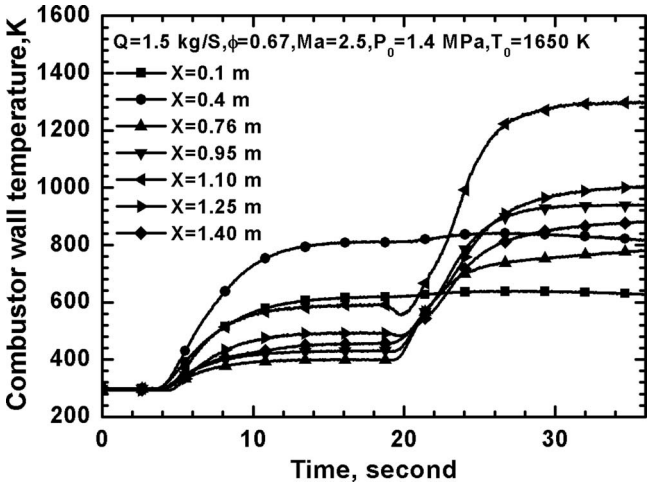

FIG. 25. Time histories of the wall temperatures along the combustor.

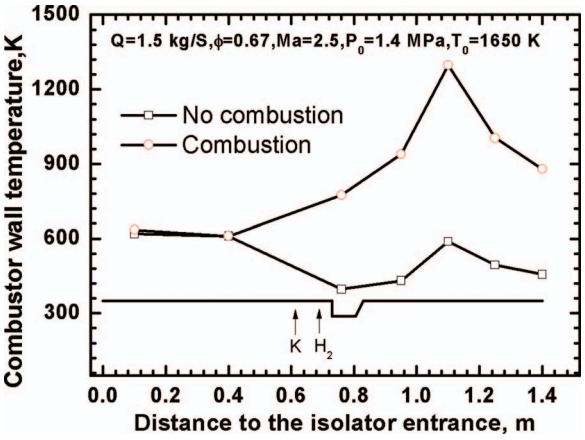

FIG. 27. Wall temperature distributions along the combustor with and without combustion.

the corresponding wall temperature distributions for the two cases. The wall temperatures with combustion is nearly twice as much as that without combustion in the combustion region. Most of the sensors survived after about 50 runs and the outputs showed very good repeatability.

VI. CONCLUSION

A water-cooled heat flux/wall temperature measurement technique has been developed based on the principle of Gardon heat-flux sensor. Heat resistance analysis has been used to design the thermal structure of the sensor. Numerical simulation of the heat conduction inside the sensor structure demonstrated that the output of the sensor was linearly proportional to the applied heat flux and a maximum heat flux of 400 W/cm^2 could be measured using this sensor. Effects of materials and structure on the sensor's responses have also been examined. The response time of sensor is comparable with Gardon gauge. Calibration processes using radiative and conductive heating sources were carried out and calibration profile of heat flux vs. voltage as well as wall temperature vs. heat flux were obtained. Calibration at higher heat flux was carried out using a blackbody cavity. The successful measurements in a supersonic model combustor showed that the new developed sensors had wider measurement range and fast response, satisfactory accuracy and precise, as well as enough durability.

ACKNOWLEDGMENTS

Current research program at the Chinese Academy of Sciences (CAS) was supported by the National Natural Science Foundation of China (NNSFC) under Contract Nos. 91016005 and 10621202. The authors would like to acknowledge Mr. J. Q. Wang, X. S. Wei, P. Huang, Y. Li, and L. J. Meng for their technical support.

[1]J. Ewing, A. Gifford, D. Hubble, P. Vlachos, A. Wicks, and T. Diller, Meas. Sci. Technol. **21**, 105201 (2010).
[2]C. T. Kidd and J. C. Adams, J. Spacecr. Rockets **38**, 719 (2001).
[3]A. H. Epstein, G. R. Guenette, R. J. G. Norton, and Y. H. Cao, Rev. Sci. Instrum. **57**, 639 (1986).
[4]N. E. Hager, Rev. Sci. Instrum. **36**, 1564 (1965).
[5]S. Löhle, J. L. Battaglia, P. Jullien, B. van Ootegem, J. Couzi, and J. P. Lasserre, J. Spacecr. Rockets **45**, 76 (2008).
[6]W. K. George, W. J. Rae, and S. H. Woodward, Exp. Therm. Fluid Sci. **4**, 333 (1991).
[7]C. H. Liebert, R. Holanda, S. A. Hippensteele, and C. A. Andracchio, ASME J. Eng. Gas Turbines Power **107**, 938 (1985).
[8]M. S. Jan, K. Sebastian, and H. Klaus, in *Proceedings of the 15th AIAA International Space Planes and Hypersonic Systems and Technologies Conference*, Dayton, Ohio, 2008, 2547.
[9]A. D. Gardner, K. Hannemann, A. Paull, and J. Steelant, in *Proceedings of the 24th International Symposium on Shock Waves*, Beijing, China, 2005.
[10]A. Ferriere and B. Rivoire, Sol. Energy **72**, 187 (2002).
[11]J. Ballestrin, M. Rodriguez-Alonso, J. Rodriguez, I. Canadas, F. J. Barbero, L. W. Langley, and A. Barnes, Metrologia **43**, 495 (2006).
[12]J. R. Filtz, T. Valin, J. Hameury, and J. Dubard, Int. J. Thermophys. **30**, 236 (2009).
[13]D. G. Holmberg, C. A. Womeldorf, and W. L. Grosshandler, in Proceedings of the The ASME International Mechanical Engineering Congress and Exposition, Nashville, TN, 1999.
[14]W. L. Grosshandler and D. Blackburn, in Proceedings of the 1997 ASME International Mechanical Engineering Congress and Exposition, Dallas, TX, 1997.
[15]A. V. Murthy, B. K. Tsai, and C. E. Gibson, J. Res. Natl. Inst. Stand. Technol. **102**, 479 (1997).
[16]A. V. Murthy, B. K. Tsai, and R. D. Saunders, Metrologia **35**, 501 (1998).
[17]A. V. Murthy, B. K. Tsai, and R. D. Saunders, J. Res. Natl. Inst. Stand. Technol. **104**, 487 (1999).
[18]A. V. Murthy, B. K. Tsai, and R. D. Saunders, J. Res. Natl. Inst. Stand. Technol. **105**, 293 (2000).
[19]A. V. Murthy, B. K. Tsai, and R. D. Saunders, J. Res. Natl. Inst. Stand. Technol. **106**, 823 (2001).
[20]B. K. Tsai, C. E. Gibson, A. V. Murthy, E. A. Early, D. P. Dewitt, and R. D. Saunders, National Institute of Standards and Technology (NIST) Special Publication 250-65, 2004.
[21]A. V. Murthy, A. V. Prokhorov, and D. P. DeWitt, J. Thermophys. Heat Transfer **18**, 333 (2004).
[22]A. V. Murthy, G. T. Fraser, and D. P. DeWitt, J. Thermophys. Heat Transfer **20**, 327 (2006).
[23]A. N. Abdelmessih and T. J. Horn, ASME Trans. J. Heat Transfer **132**, 023304 (2010).
[24]R. Gardon, Rev. Sci. Instrum. **24**, 366 (1953).
[25]IEC584-1, International Standard, Thermocouple-Part 1: Reference tables, 1995.